


Alginate/Gelatin Hydrogel Scaffold Containing nCeO₂ as a Potential Osteogenic Nanomaterial for Bone Tissue Engineering

Feng Li^{1,2}, Jian Li^{1,2}, Xujun Song^{1,2}, Tong Sun³, Lian Mi^{1,2}, Jian Liu^{1,2}, Xiaomin Xia^{1,2}, Na Bai^{1,2},
Xue Li^{1,2} 

¹Department of Stomatology, The Affiliated Hospital of Qingdao University, Qingdao University, Qingdao, 266003, People's Republic of China;

²School of Stomatology, Qingdao University, Qingdao, 266071, People's Republic of China; ³College of Chemistry and Chemical Engineering, Qingdao University, Qingdao, 266071, People's Republic of China

Correspondence: Na Bai; Xue Li, Tel +86-15621438983, Email na.bai@qdu.edu.cn; lixue@qdu.edu.cn

Background: Clinicians frequently face difficulties when trying to fix bone abnormalities. Gelatin-Alginate (GA) is frequently employed as a carrier because it is non-toxic, biodegradable, and has a three-dimensional network structure. Meanwhile, cerium oxide nanoparticles (nCeO₂) demonstrated high antioxidant enzyme simulation activity. Therefore, in order to develop a porous hydrogel scaffold for the application of bone tissue engineering, an appropriate-type GA-nCeO₂ hydrogel scaffold was developed and evaluated.

Methods: GA-nCeO₂ hydrogel scaffold was prepared by the lyophilized method and characterized. The surface morphology and cell adhesion of the scaffold were observed by the scanning electron microscope. CCK8 and live-dead staining methods were used to evaluate its biological safety and cell proliferation. Then the osteogenic differentiation in early and late stages was discussed. The expression of osteogenic genes was also detected by RT-PCR. Finally, a bone defect model was made in SD rats, and bone formation in vivo was detected.

Results: The results showed that GA-nCeO₂ hydrogel scaffold exhibited a typical three-dimensional porous structure with a mean pore ratio of 70.61 ± 1.94%. The GA-nCeO₂ hydrogel was successfully endowed with simulated enzyme activity including superoxide dismutase (SOD) and catalase (CAT) after the addition of nCeO₂. Osteoblasts demonstrated superior cell proliferation and adhesion on composite scaffolds, and both mineralization test and gene expression demonstrated the strong osteogenic potential of GA-nCeO₂ hydrogel. The outcomes of hematoxylin and eosin (H&E) staining and Masson trichrome staining in the femoral defect model of SD rats further supported the scaffold's favorable biocompatibility and bone-promoting capacity.

Conclusion: Due to its favorable safety, degradability, and bone formation property, GA-nCeO₂ hydrogel was anticipated to be used as a potential bone defect healing material.

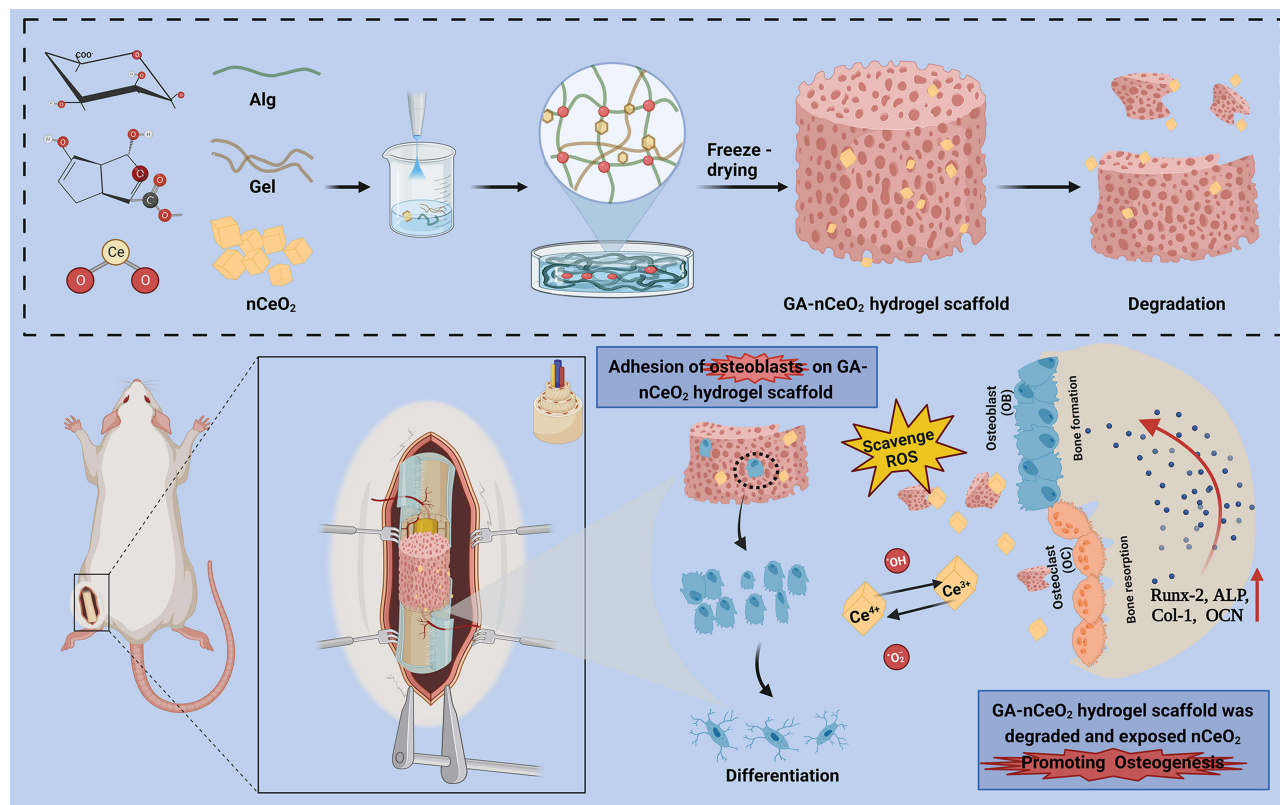
Keywords: bone regeneration, cerium oxide nanoparticles, hydrogel, bone defect

Introduction

Bone is a natural composite material that continuously remodels throughout the course of a person's life.¹ It is commonly accepted that infections, tumor excision, and trauma can result in bone abnormalities. According to an epidemiological study, orthopedic surgeons are facing a serious issue as a result of the rising prevalence of bone abnormalities.² For treating bone damage brought on by trauma or illness, materials with particular mechanical and chemical qualities have grown to be crucial over time.

Hydrogel as a polymer has a three-dimensional network structure and adjustable physical and chemical properties.³ As skin burn dressings, natural polymers like collagen and turtle chondrocytes have been fixed on hydrogels.⁴ Wang and Rhim produced hydrogel films by combining agar, alginate, and collagen with silver nanoparticles or grapefruit seed extract.⁵ This discovery may be attributed to the favorable properties of hydrogels, including biocompatibility, biodegradability, and structural resemblance to human tissue.⁶ Alginate (Alg) is an anionic polysaccharide that is both non-toxic and

Graphical Abstract



biodegradable.^{7,8} Gelatin (Gel) is widely used in the biomedical field because of its advantageous qualities, such as biodegradability.^{9–11} In addition, Gel also encourages cell adhesion and proliferation.^{12,13} Common hydrogels like Alg and Gel were usually cross-linked with divalent cations like Ca^{2+} , which do not provide cell adhesion ligands but instead promote cell attachment and differentiation.¹⁴ The cross-linked alginate-gelatin (GA) hydrogel has a stable three-dimensional network structure and is a viable biomaterial for bone repair, as demonstrated by the creation of an injectable GA scaffold.¹⁵ Additionally, it has been demonstrated that adding Alg to Gel hydrogel could improve material toughness without significantly changing Young's modulus.¹⁶ At the same time, the incorporation of nanoparticles could slightly enhance the mechanical characteristics and stability.¹⁷ Previous research in the area of bone regeneration has shown that a hydrogel scaffold made primarily of collagen and hyaluronic acid provides an environment that closely resembles the extracellular matrix of cartilage and could be utilized to repair cartilage defects.¹⁸ Hydrogels are extensively used in the medical field, while their application in tissue engineering is limited by their poor mechanical strength. However, studies have shown that employing naproxen as the drug coating and Alg and Gel as the raw ingredients, a unique soft and hard tissue regeneration scaffold was produced. Drug coating increased the polymer adhesion, as well as gained the hardness of chemical bonds.¹⁹

Even though composite hydrogels made from Gel and Alg are three-dimensional network polymers with the ability to absorb and store water as well as have strong cell adhesion and safety, they do not have a great deal of potential for enabling bone.¹⁶ Whatever the case, hydrogels are often used as scaffolds to load nanoparticles. For instance, it has been proposed that the usage of cross-linked chitosan-Gel and Fluorohydroxyapatite bioceramics that have been freeze-dried at -76°C for 48 h can aid in bone regeneration.²⁰ Nanoparticle concentration could boost scaffold compressive strength while lowering the penetration rate. Additionally, Alg-hydroxyapatite-coated porous bone scaffolds had improved cell activity, decreased porosity, and higher mechanical strength, making them better suited for use as bone scaffolds.²¹

Due to their unique catalytic activity, cerium oxide nanoparticles ($n\text{CeO}_2$) have recently gained increasing interest in biomedical applications. By observing alterations in the local tissues and major organs following subcutaneous implantation of $n\text{CeO}_2$ for 28 days in rats, the safety of $n\text{CeO}_2$ was investigated.²² The findings showed that $n\text{CeO}_2$ have no detrimental impact on important organs and do not considerably stimulate local tissues, proving their biological safety. As an effective treatment for diseases brought on by free radicals or oxidative stress, $n\text{CeO}_2$ has drawn a lot of interest.²³ It is interesting to note that during redox processes, $n\text{CeO}_2$ could quickly change the oxidation state between Ce^{4+} (CeO_2) and Ce^{3+} (Ce_2O_3).²⁴ Moreover, due to their antioxidant capacity, $n\text{CeO}_2$ are considered to be efficient reactive oxygen species (ROS) scavengers, and ROS are crucial to the homeostatic balance of bone.²⁵ It has been claimed that $n\text{CeO}_2$ could promote osteogenic differentiation via stimulating M2-type macrophage differentiation together with mesenchymal stem cell differentiation.²⁶ In addition to aligning the development of stem cells, $n\text{CeO}_2$ also increased the polymer scaffold surface's bioactivity to encourage cell adhesion.²⁷ Similarly, composite scaffolds containing $n\text{CeO}_2$ dramatically enhanced bone repair.²⁸ According to studies, covering implants with $n\text{CeO}_2$ could boost bone mesenchymal stem cell osteogenic activity and encourage osteoblast growth.²⁹ These findings offer fresh proof of Ce's bone metabolism process as well as fresh concepts for the future practical use of $n\text{CeO}_2$.

Given the advantageous characteristics of Gel, Alg, and $n\text{CeO}_2$, we sought to determine if gelatin-alginate nanocomposite cerium (GA- $n\text{CeO}_2$) hydrogel scaffold may be used in bone regeneration to increase the composites' ability to repair broken bones. By creating a particular microenvironment, the hydrogel scaffold, a porous matrix, helps to promote cartilage/osteocondral repair and regeneration.³⁰ Scaffolds should ideally be able to (1) support cell survival, proliferation, and differentiation; (2) have an appropriate mechanical strength; (3) degrade at a specific rate; (4) be biocompatible. As depicted in Graphical abstract, we aimed to confirm the efficient production of GA- $n\text{CeO}_2$ nanocomposite lyophilized hydrogel scaffold and investigate its features, physical properties, capacity for osteogenic differentiation, and in vivo biocompatibility.

Materials and Methods

Materials

All reagents including alginate ($M_w = 600 \text{ Kg/mol}$, $M/G = 1.2$, the viscosity is $200 \text{ mPa}\cdot\text{s}$), gelatin and CaCl_2 , NaOH , phosphate-buffered saline (PBS), Bicinchoninic Acid (BCA) Protein Assay Kit (Meilunbio), and all cell culture reagents were available from Solarbio. Aladdin's $\text{Ce}(\text{NO}_3)_3 \cdot 6\text{H}_2\text{O}$ was employed as the starting compound. Cell culture investigations were conducted using MC3T3-E1. Jiancheng Bioengineering Institute provided the Alizarin red stain (ARS) and alkaline phosphatase (ALP) assay kit.

Cerium Oxide Nanoparticle ($n\text{CeO}_2$) Synthesis

$n\text{CeO}_2$ was synthesized using $\text{Ce}(\text{NO}_3)_3 \cdot 6\text{H}_2\text{O}$ as a starting material. $0.5 \text{ g Ce}(\text{NO}_3)_3 \cdot 6\text{H}_2\text{O}$ was dissolved in 10 mL deionized water and 18 g of NaOH in 30 mL deionized water, respectively. Subsequently, the aqueous $\text{Ce}(\text{NO}_3)_3$ solution was transferred to a stainless-steel autoclave lined with Teflon, followed by the dropwise addition of liquid NaOH and stirring for 10 min . The autoclave was then sealed and kept in a furnace at 150°C for 24 h . The precipitate was separated and collected by centrifugation, followed by alternate washing with deionized water and anhydrous ethanol, and finally dried at 100°C to a yellow powder.

Preparation of GA Containing $n\text{CeO}_2$

The GA with $n\text{CeO}_2$ scaffolds was prepared by freeze-drying. 2% Alg solution and 10% Gel solution were prepared and then mixed to get the GA polymer mixture. To prepare nanoparticle-containing scaffolds, $1000 \mu\text{g/mL}$ $n\text{CeO}_2$ was added to the blend. The scaffolds were cross-linked with calcium chloride solution (8%). In the final step, the scaffolds were cleaned and freeze-dried. Alginate alone, pure gelatin and $n\text{CeO}_2$ alone, gelatin/alginate mix, and gelatin/alginate with $n\text{CeO}_2$ denoted as Alg, Gel, $n\text{CeO}_2$, GA, and GA- $n\text{CeO}_2$ hydrogel scaffold, respectively. Additionally, equal volumes of Gel, Alg, GA, and GA- $n\text{CeO}_2$ solutions were cast onto the pore plates to obtain the same diameter and thickness of scaffolds.

Material Characterization and Physical Properties

Dynamic Light Scattering and Zeta Potential Analysis

Nanoparticle Tracking Analysis and Dynamic Light Scattering (DLS) were carried out in suspensions. The zeta potentials of nCeO₂ were measured by Zetasizer (Malvern Zetasizer Nano ZS90) DLS method. The zeta potential and average particle size of nanoparticles were obtained by analysis. In triplicate, take the average value. The results were expressed by mean ± standard deviation (SD).

X-Ray Diffraction, X-Ray Photoelectron Spectroscopy, and Fourier Transform Infrared

X-ray diffractometry (XRD, Bruker AXS) was used to examine the XRD patterns of the five groups: Alg, Gel, nCeO₂, GA, and GA-nCeO₂ hydrogel scaffold, respectively. The surface chemical makeup and valence of nCeO₂ and GA-nCeO₂ hydrogel scaffold were assessed using X-ray photoelectron spectroscopy (XPS, Thermo Fisher Scientific). The specific functional groups in the hydrogels were determined by Fourier transform infrared (FTIR, Thermo Fisher) analysis, with spectra recorded in the range of 4000 to 600 cm⁻¹.

Transmission Electron Microscope and Scanning Electron Microscope

Transmission electron microscopy (TEM, FEI TalosF200x) was used to characterize the size and shape of nCeO₂. After spraying gold on the cross-section of the scaffold, the surface morphology of composite scaffolds was observed by scanning electron microscope (SEM). The main porosity of the scaffold was automatically calculated from SEM images using ImageJ software.

Analysis of the Catalytic Mimetic Activity of Alg, Gel, nCeO₂, GA, and GA-nCeO₂ Hydrogel Scaffold

The Total Superoxide Dismutase (SOD) Assay Kit with WST-8 (S0101, Beyotime) was used by the manufacturer's instructions to measure the SOD activity of Alg, Gel, nCeO₂, GA, and GA-nCeO₂. Absorbance was gauged at 450 nm. The peroxidase activity of nCeO₂ and freeze-dried scaffold was assessed using a catalase (CAT) activity assay kit (S0051, Beyotime). The absorbance was measured at 450 nm.

Swelling Study

The lyophilized hydrogel samples were weighed as (W_0) and impregnated with 3 mL PBS (pH 7.4) to determine hydrogel swelling, and swelling was allowed to persist for 48 h to achieve equilibrium. After absorbing the excess solution on the hydrogel scaffold with filter paper, the swollen scaffold was weighed as (W_1). Finally, the swelling ratio of hydrogels was calculated using the following formula: swelling ratio (%) = $(W_1 - W_0) / W_0 \times 100\%$.

Degradation Behavior

The initial mass of the hydrogel (W_0) was measured precisely. Subsequently, the lyophilized hydrogel samples were submerged in 5 mL of PBS (0.01 M, pH 7.4) and incubated at 37°C. The scaffold was then separated from PBS and lyophilized, and their final weight (W_t) was measured. The experiments were performed in triplicate. The extent of in vitro degradation was calculated using the following equation: remaining (%) = $W_t / W_0 \times 100\%$.

Mechanical Testing

The compression modulus of the hydrogel (25 mm diameter, 10 mm thickness) was evaluated using a universal testing machine at room temperature. All hydrogel samples were compressed at a displacement rate of 2 mm/min. The compression modulus was determined by linearly fitting stress–strain curves.

In vitro Biocompatibility

All cell culture-related studies used scaffolds of the same shape (cylindrical) and size. For sterilization, the scaffold was soaked in 75% ethanol in the presence of ultraviolet (UV) light for 1 h, and then the scaffold was cleaned with PBS.³¹

Cell Culture on Hydrogels

We used MC3T3-E1 cells to study the effects of proliferation and differentiation of hydrogel scaffolds. Cells were cultured in Dulbecco's modified Eagle medium containing 10% fetal bovine serum and 1% penicillin and streptomycin at

37°C and 5% CO₂. On day 3, the medium was changed, and when the cell density reached 80%, the cells were separated with 1% (w/v) trypsin-EDTA, and the digested cells were used for further experiments. To further study osteoblastic differentiation in vitro, dexamethasone, sodium glycerol β -phosphate, and L-ascorbic acid were added to the medium to prepare an osteoinductive medium.

Cell Morphology and Proliferation on GA-nCeO₂ Hydrogel Scaffold

MC3T3-E1 cells were cultured on different groups for 3 days, and their morphology was observed by SEM. Cell proliferation on hydrogel was further assessed by the CCK-8 assay, a colorimetric method for determining the number of viable cells. Cells were inoculated into 96-well plates with approximately 100 μ L of cell suspension per well at each time point (1, 2, and 3 days). 10 μ L of CCK-8 solution was added to each well and incubated at 37°C for 1 h. The optical density (OD) at 450 nm was measured using a spectrophotometer (HBS-1069A). Five parallel lines were available for each sample, and the average was taken.

Additionally, Live/Dead staining was used to assess the cytocompatibility of the hydrogel lyophilized scaffolds. The Alg, Gel, GA, and GA-nCeO₂ hydrogel scaffold were, respectively, submerged in the culture medium for 24 h at 0.1 g/mL to produce the leaching solution. 5000 cells/well were used to cultivate the cells on 48-well plates, which were then stained on the third day with a Live/Dead Cell Double Staining Kit (Meilunbio). After staining the cells after 30 min of dark incubation, 300 μ L PBS was used to wash them. In the end, an inverted fluorescent microscope was used to view the cells.

Osteogenic Differentiation of Preosteoblasts on GA-nCeO₂ Hydrogel Scaffold

ALP Activity Measurements and Cell Mineralization

ALP is commonly used as a marker for osteogenesis. The activity and total protein concentration of ALP were evaluated using ALP kits according to the manufacturer's protocol. In summary, MC3T3-E1 cell suspension was added to 24-well culture plates (at a density of 1×10^5 cells/well) with different hydrogel scaffolds at the bottom of each well. On days 7 and 14, cells were collected for relative quantification of ALP. ALP levels were assessed using a colorimetric method at 405 nm and normalized to total protein content. For ALP staining, scaffolds containing cells at 7 days were washed with PBS, fixed in 4% paraformaldehyde, and stained with the Bicinchoninic Acid (BCA) Protein Assay Kit (Meilunbio). To evaluate the mineralization of hydrogels, on days 14 and 21 of osteogenesis induction, fixed with 4% paraformaldehyde for 30 min, and then stained with ARS. They were observed under a microscope and photographed. 1 mL of cetylpyridinium chloride was added to each well and incubated for 15 min at room temperature to dissolve the calcium nodules. The OD value was measured at a wavelength of 540 nm with an enzyme marker.

Osteogenic Gene Expression

To evaluate the bone formation induction, we measured osteogenesis-related gene expression levels (runt-related transcription factor 2 (Runx-2), alkaline phosphatase (ALP), collagen1 (Col-1), osteocalcin (OCN), and β -actin using real-time PCR. Briefly, RNA was extracted from hydrogel-cultured cells using Trizol reagent (Invitrogen). After that, RNA was reverse transcribed into cDNA using PrimeScriptTM RT Reagent Kit (Takara). A Bio-Rad iCycler Real-time PCR System was used to amplify and quantify target gene cDNA levels. The gene expression levels of each sample were calculated using the $2^{-\Delta\Delta Ct}$ method, which was repeated three times. The primer sequences are shown in Table 1.

Table 1 Primer Sequences Used for qRT-PCR

Gene	Forward Sequence	Reverse Sequence
ALP	GGCAAAGAGGGAGCTAGAA	ATGGCCGTGCAGATGTA
OCN	AGCAGGAGGGCAATAAGGT	GCTTTAGGGCAGCACAGG
Runx-2	CCTCCAGCATCCCTTTCTT	CCTTTTCCCTCCTTGCCCT
Col-1	GACATGTTTCAGCTTTGTGGACCTC	GGGACCCTTAGGCCATTGTGTA
β -actin	CATCCGTAAGACCTCTATGCCAAC	ATGGAGCCACCGATCCACA

In vivo Animal Studies

Femoral defect models were created in 8-week-old male SD rats following a protocol approved by the Institutional Animal Ethics Committee of Qingdao University Laboratory Animal Center (20210708SD1520210920064) and were conducted in strict accordance with the guidelines for Ethical Review of Laboratory Animal Welfare in China (GB/T35892-2018). Briefly, the rat was anesthetized by isoflurane inhalation, a 2 cm linear incision was made in the proximal femur. A single cortical defect, 2 mm wide and 4 mm long, was created on the lateral aspect of both sides of the femur. After creating the femoral defect, the left area was filled with a pre-designed scaffold. The right area is the blank group. After surgery, the rats were administered 3% penicillin and kept in separate cages. At postoperative weeks 4, 6, and 8, the left femurs with the implanted composite were harvested for microcomputed tomography (micro-CT) analysis, and the harvested femur samples were fixed in 4% paraformaldehyde, followed by micro-CT testing, and hematoxylin and eosin (H&E) and Masson staining.

Statistical Analysis

Data were expressed as mean \pm SD and analyzed with SPSS (SPSS Inc., Chicago, IL). One-way ANOVA and Tukey's multiple comparison test were used to assess differences between groups, and p values <0.05 were statistically significant.

Results and Discussion

Characterization of nCeO₂

In this study, nCeO₂ were synthesized by the coprecipitation method, and TEM and DLS analysis were used to examine their morphology and size. Zeta potential was assessed after the ultrasonic pulse had suspended nCeO₂. The cubic nature of the generated nCeO₂ was confirmed by TEM, as shown in Figure 1A. According to DLS data, nCeO₂ has an average particle size of 22.13 ± 1.21 nm and a zeta potential of -19.1 ± 1.31 mV (Figure 1B and C). The high surface charge of nanoparticles causes repulsive force, which makes it difficult for them to recombine and maintain the created nanoparticles in a stable state.³²

The synthetic nCeO₂'s X-ray diffraction pattern's peaks closely matched the typical cerium pattern (PDF2: 34-0394), confirming the extraordinary purity of the nanoparticles we made (Figure 1D). As shown in Figure 1E, Ce 3d_{3/2} of 916.68, 907.75, and 901.4 eV for CeO₂ and Ce 3d_{5/2} of 898.82, 888.04, and 882.76 eV for CeO₂ (solid line); Ce 3d_{3/2} of Ce₂O₃ 904.27 and 899.23 eV for Ce₂O₃ and 885.02 and 880.7 eV for Ce 3d_{5/2} (dashed lines). Figure 1F shows the relative evolution of the Ce 3d XPS spectra of the nCeO₂. The corresponding quantitative results for the valence concentration ratios shown in the figure indicating the ratio of surface Ce⁴⁺ (CeO₂) to surface Ce³⁺ (Ce₂O₃) was 61.49% to 38.51%. According to the XPS data, Ce⁴⁺ predominates in the valence state, and a small number of Ce³⁺ coexist with Ce⁴⁺. As a result of this coexistence, nCeO₂ is crucial in catalytic and biological processes based on electron transport pathways.³³ Because it could switch between Ce³⁺ and Ce⁴⁺, nCeO₂ was exceptional in redox chemistry. This property makes nCeO₂ comparable to biological antioxidants like CAT and SOD, and it is essential for the elimination of ROS such as the superoxide radical (O₂^{•-}) and hydrogen peroxide (H₂O₂).³⁴

ROS has come under scrutiny as a possible etiology for metabolic bone diseases. CAT, an enzyme scavenger, may break down H₂O₂ into molecular oxygen and water in vivo to safeguard cells from the toxicity of H₂O₂. It plays a crucial role in the body's defense system as an enzyme. The vital free radical scavenger SOD helps the body defend itself against oxidative damage by removing excess superoxide anion radicals, such as O₂^{•-}. The catalytic action of nCeO₂ on SOD is accomplished through the alternating electron gain and loss of Ce⁴⁺ (oxidized state) and Ce³⁺ (reduced state).^{34,35} After the superoxide anion radical first forms an inner boundary complex with nCeO₂, Ce⁴⁺ is reduced to Ce³⁺ by the superoxide anion radical, which also generates O₂^{•-}, and Ce³⁺ is oxidized to Ce⁴⁺ by HO₂[•], which also generates H₂O₂. Additionally, nCeO₂ might function as a reductase, a mechanism similar to the conversion of electrons from Ce⁴⁺ to Ce³⁺. Then nCeO₂ mimics the CAT enzyme, which could catalyze the decomposition of H₂O₂ into H₂O and O₂. The process could be divided into two steps: 1) H₂O₂ was used as a reducing agent to transfer two H atoms to nCeO₂, and H₂O₂ is oxidized to O₂ to leave, thus obtaining the active intermediate H₂-CeO₂. 2) Then H₂O₂ can be used as an oxidant

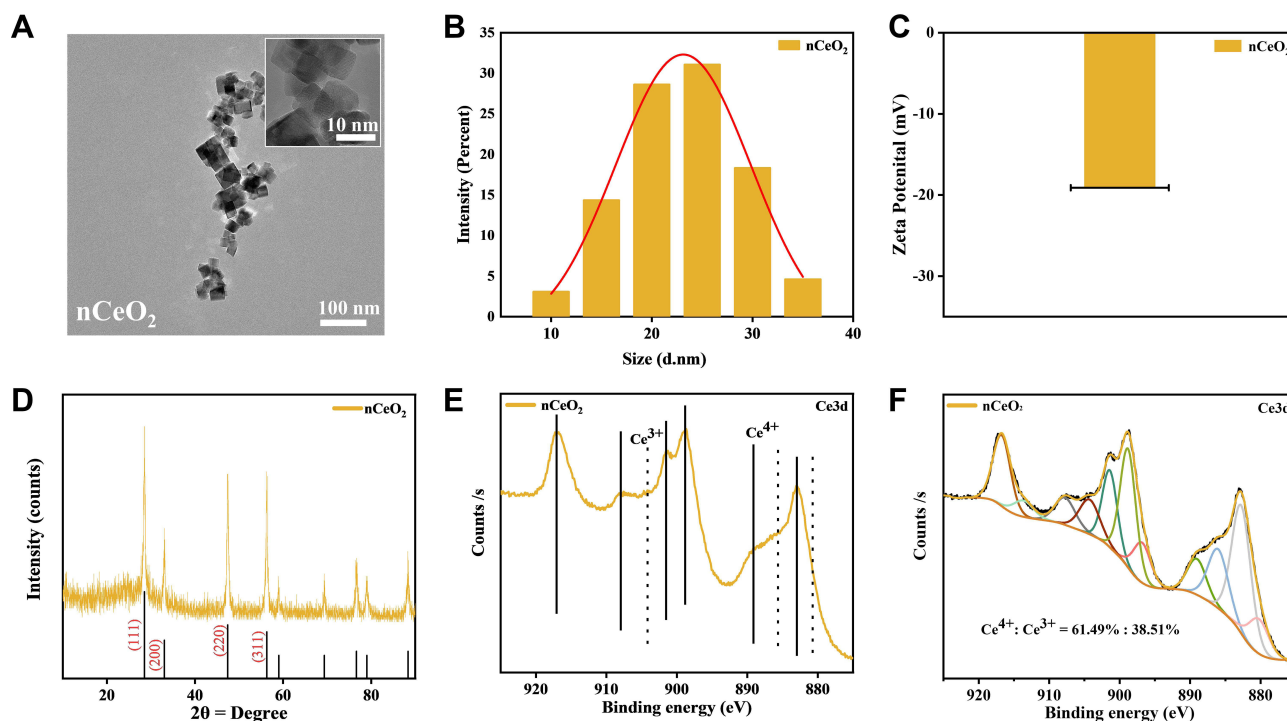


Figure 1 Characterization of nCeO₂. **(A)** TEM images of nCeO₂; **(B)** Particle size distribution of nCeO₂; **(C)** Zeta potential analysis of nCeO₂; **(D)** XRD analysis of nCeO₂; **(E)** XPS analysis for the coexistence of Ce³⁺ and Ce⁴⁺ in the nCeO₂; **(F)** XPS analysis for the ratio of Ce³⁺ and Ce⁴⁺ in the nCeO₂.

to capture H atoms in the active intermediate H₂-CeO₂, and H₂O₂ is reduced to H₂O to leave.³⁶ The SOD and CAT enzymes' abilities to scavenge ROS could be mimicked by the redox cycle between Ce³⁺ and Ce⁴⁺.

Characterization of GA-nCeO₂ Hydrogel Scaffold

In order to examine the microstructure of the lyophilized hydrogel, a SEM was employed. Figure 2A–D illustrated how each scaffold had a typical three-dimensional porous structure with pore walls that were relatively related to one another, promoting cell adhesion and extension. Figure 2E, an enlarged view of the red dashed box in Figure 2D, clearly showed the uniformly distributed nCeO₂ attached to the scaffold material, while the interpolation showed the transmissive structure of the cube nCeO₂ attached to the scaffold. It has been demonstrated that freeze-drying could be used to homogenize nanoparticles in natural biopolymers and create porous biological nanocomposites with ordered porosity distribution and honeycomb structure.^{37,38} The possibility of implanting bioactive scaffolds into bone tissue now has a new source. Given their major effects on angiogenesis and bone tissue formation, the pore size and porosity of hydrogel are recognized as key elements in bone tissue engineering.^{8,29} As shown in Figure 2F, the mean pore ratio of Alg, Gel, GA, and GA-nCeO₂ hydrogel scaffolds was 59.21 ± 3.21%, 71.20 ± 2.41%, 67.38 ± 1.57%, and 70.61 ± 1.94%, respectively. The GA scaffold's porosity did not alter significantly from the GA scaffold's porosity following the addition of nCeO₂. There is strong evidence that a scaffold's porosity should be between 50% and 90% to achieve the desired biological and physical properties,^{4,5,20} and the fact that GA-nCeO₂ scaffolds fall within this range might be one of the arguments in favor of the scaffold material as a potential candidate for bone tissue engineering.³¹

The structure and components of the composite scaffold are deciphered in Figure 3A. Figure 3B shows the XRD patterns of Alg, Gel, nCeO₂, GA, and GA-nCeO₂ hydrogels. The XRD pattern of Alg hydrogels showed two narrower at 32.0° and 47.1° diffraction peaks and the Gel hydrogels exhibited strong reflection at 20–21°, which was corresponding to a short-range ordered structure.³⁹ As previously mentioned (Figure 1D), the XRD patterns of nCeO₂ were consistent with the typical cerium oxide pattern. These unique XRD peaks were defined by their respective indices (111), (200), (220), (311), (222), (400), and (420).^{40,41} The diffraction peaks of Gel and Alg mixed with nCeO₂ broadened significantly and moved to lower 2θ. The addition of GA caused the peaks of the GA-nCeO₂ hydrogel to weaken at

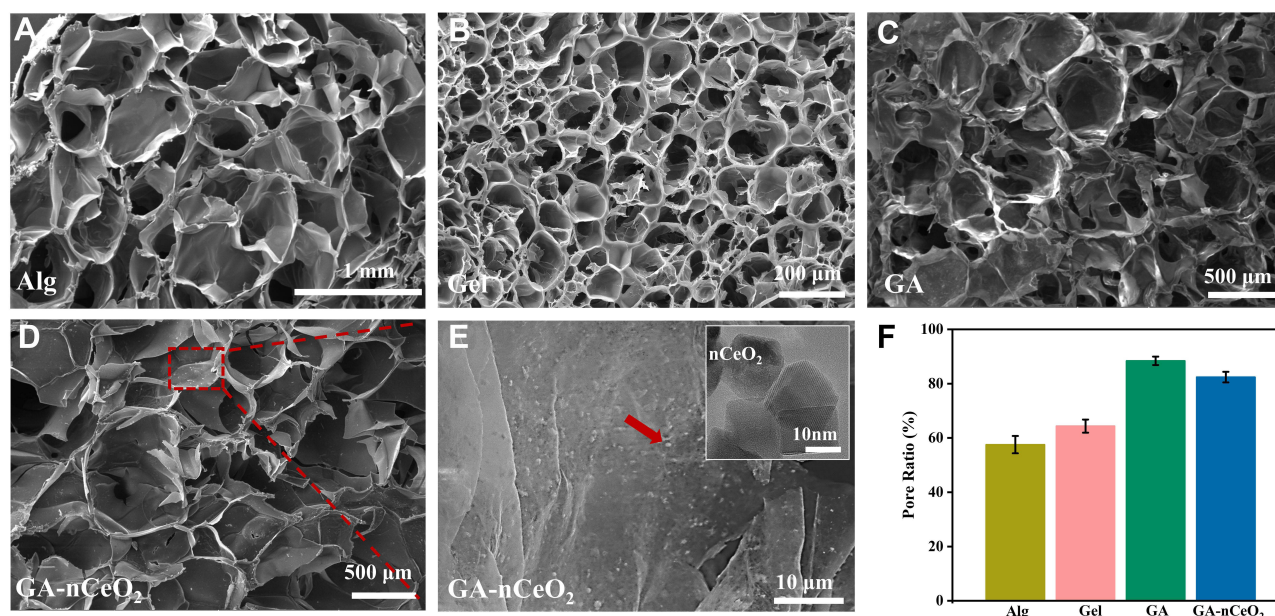


Figure 2 SEM images and porosity analysis of hydrogels: (A) Alg; (B) Gel; (C) GA; and (D) GA-nCeO₂; (D) the distribution of nCeO₂ in the GA-nCeO₂ hydrogel scaffold; (E) the enlargement of the red dashed rectangle in (D) distribution of nCeO₂ in the GA-nCeO₂ hydrogel scaffold (inset: transmission structure map of nCeO₂ shown by red arrows); (F) the porosity analysis of the Alg, Gel, GA and GA-nCeO₂ hydrogel scaffold.

the first peak while enhancing the second peak, indicating a phase transition during the composite process. FTIR spectra of Alg, Gel, nCeO₂, GA, and GA-nCeO₂ hydrogels are shown in Figure 3C. The absorption bands in the FTIR spectra were assigned to the vibrations of the corresponding functional groups based on published data for Gel^{42–44} and Alg.^{45,46} The absorption peaks at 1600 cm⁻¹ and 1415 cm⁻¹ in the pure Alg infrared spectrum were attributed to the asymmetric and symmetric stretching vibrations of the alginate groups, respectively. Moreover, absorption bands were observed at 1635 cm⁻¹ (asymmetric stretching vibration of the COO group) and 882 cm⁻¹ (extension of the nCeO₂ group). The absorption band at around 1400 cm⁻¹ represented the carboxyl group of Gel. In addition, the two absorption peaks at 1635 cm⁻¹ and 1464 cm⁻¹ correspond to the amide I and amide II bands of Gel. Typically, the background spectrum of nCeO₂ contained bands corresponding to the surface hydroxyl groups. The absorbance peak at 800 cm⁻¹ was ascribed to Ce-O bonds, which belong to crystalline cerium oxide active phonon modes in a range of 900–400 cm⁻¹.^{47–50} In addition, cerium oxide usually contains carbonates, which are thought to exist in the subsurface layer and are difficult to remove and correspond to bands in the 1600–1260 cm⁻¹ region.⁴⁸ In the physically mixed FTIR spectra of Alg and Gel, the tensile vibrational bands of the GA at 852 cm⁻¹ gradually weakened with the addition of the nCeO₂. In addition, the expansion at 3500–3000 cm⁻¹ might be due to the interaction of the hydroxide groups contained in GA with representative oxide groups contained in nCeO₂. These changes indicated a strong molecular interaction between Alg and Gel chains through the self-organization of polyelectrolyte complexes, including hydrogen bonding and electrostatic attraction.

The surface XPS survey spectrum of the GA-nCeO₂ hydrogels is displayed in Figure 3D. Ce came from nCeO₂, C and N from Alg and Gel, and Ca came from calcium chloride, a crosslinking agent. It was worth noting that the appearance of Ce indicated that nCeO₂ has been successfully added to the hydrogel scaffold. The single spectrum revealed that GA-nCeO₂ hydrogels had a double oxidation state and could change between Ce⁴⁺ and Ce³⁺, indicating that the GA-nCeO₂ hydrogels would be capable of acting as an antioxidant.

Figure 3E and F showed the SOD and CAT enzyme simulated activities of Alg, Gel, GA, nCeO₂, and GA-nCeO₂ hydrogels. According to the results, the SOD and CAT enzyme activity of nCeO₂ and GA-nCeO₂ hydrogels was significantly higher than other groups. However, the CAT activity of GA-nCeO₂ hydrogels was slightly higher than that of pure nCeO₂. Previous studies have shown that GA biocompatible hydrogel prepared with calcium chloride as an ionic crosslinking agent could improve the stability of CAT and achieve effective application.^{51,52} This might be the

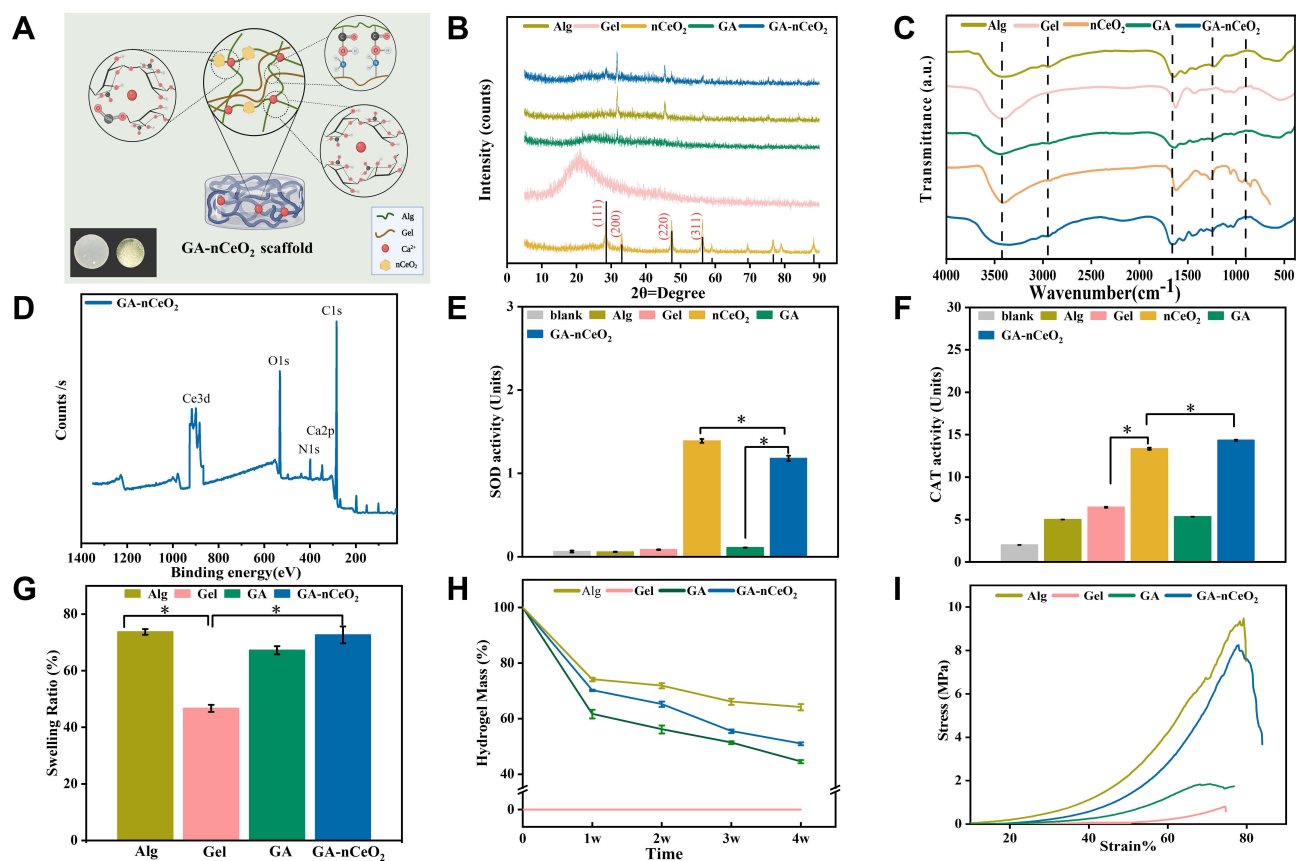


Figure 3 Material Characterization and Physical Properties: (A) The illustration of the GA-nCeO₂ hydrogel scaffold (inset: GA-nCeO₂ hydrogel scaffold before and after lyophilization). (B) XRD patterns of Alg, Gel, GA, nCeO₂ and GA-nCeO₂ hydrogel scaffold; (C) FTIR spectra of Alg, Gel, GA, nCeO₂ and GA-nCeO₂ hydrogel scaffold; (D) XPS analysis of GA-nCeO₂ hydrogel scaffold; (E) The SOD activity of Alg, Gel, GA, nCeO₂ and GA-nCeO₂ hydrogel scaffold; (F) The CAT activity of Alg, Gel, GA, nCeO₂ and GA-nCeO₂ hydrogel scaffold; (G) Equilibrium swelling studies of Alg, Gel, GA, nCeO₂ and GA-nCeO₂ hydrogel scaffold; (H) Degradation test of Alg, Gel, GA, nCeO₂ and GA-nCeO₂ hydrogel scaffold; (I) Mechanical properties of Alg, Gel, GA, nCeO₂ and GA-nCeO₂ hydrogel scaffold (stress-strain curve). The asterisks indicate a statistically significant difference between the two groups (**p* < 0.05).

reason why the CAT enzyme activity of GA-nCeO₂ was higher than that of other groups. The SOD activity of GA-nCeO₂ hydrogels was slightly lower than that of pure nCeO₂. This might be a result of the presence of hydrogel scaffold affecting the direct interaction between the incorporated nCeO₂ and the enzyme substrate.

Excessive and persistent ROS levels could cause oxidative stress to limit the regeneration of healthy bone tissue.⁵³ Additionally, oxidative stress could cause the death of osteoblasts and osteocytes, as well as prevent the osteoblast differentiation of bone marrow progenitor cells.³⁴ The most prevalent antioxidant enzymes that help shield cells from free radicals are SOD, CAT, and glutathione peroxidase.⁵⁴ As a new antioxidant biomaterial, nCeO₂ might be able to neutralize dangerous free radicals and restore the redox equilibrium of healthy cells due to its both SOD and CAT enzyme activity.^{36,51} Therefore, GA-nCeO₂ hydrogel could be able to eliminate ROS, encourage cell division, differentiate into osteoblasts with osteoinductivity, and defend osteoblasts from harm.

Physical Properties of GA-nCeO₂ Hydrogel Scaffold

Another significant factor affecting the mechanical properties of gels is the hydrogels' tendency to swell.^{55,56} From the SEM images (Figure 2D), the component lyophilized hydrogel scaffolds contained interconnected pores, which demonstrated good swelling capabilities. As shown in Figure 3G, the mean swelling rates of Alg, Gel, GA, and GA-nCeO₂ hydrogel scaffolds were, respectively, 72.68 ± 2.31%, 45.39 ± 3.18%, 65.86 ± 3.78%, and 70.00 ± 4.58%. Figure 3G has also illustrated how the swelling rate was significantly reduced, supporting the idea that Gel could influence the swelling rate of hydrogels.

The in vitro degradation of hydrogel lyophilized scaffolds is shown in Figure 3H. After 28 days, the percentage degradation of Alg, GA, and GA-nCeO₂ hydrogels was $45.32 \pm 0.52\%$, $63.71 \pm 0.56\%$, and $56.33 \pm 1.12\%$, respectively. According to reports, the scaffold structure's inclusion of Gel speeds up deterioration.⁵⁷ It is generally known that hydrogels can only be successfully employed as scaffolds for bone tissue engineering if they degrade at the right rate.⁵⁸ In this respect, it has been shown that the degradation of GA and GA-nCeO₂ scaffolds was higher than that of Alg but lower than that of Gel. The high crosslinking density of the hydrogels hinders lysozyme activity due to the addition of divalent cations, reducing the rate of Gel-induced biodegradation.⁵⁹ The structure of GA became more complete with the addition of nCeO₂, which was likely a result of enhanced intermolecular cross-linking and made it challenging for the enzyme to access the attack site in the gel structure. This result suggested that nCeO₂ might be added to GA to lessen the deterioration of hydrogels brought on by the addition of Gel. Hydrogel scaffold needed certain degradation ability, so that nanoparticles could be released and exert their double oxidation.^{60,61}

For bone tissue engineering, scaffolds with appropriate mechanical properties were needed, especially compressive strength, as shown in Figure 3I. At 80% strain, the compressive strengths of Gel, Alg, GA, and GA-nCeO₂ hydrogels were 1.29 MPa, 9.75 MPa, 2.35 MPa, and 8.46 MPa, respectively. As previously noted, the addition of nCeO₂ resulted in the formation of an integral GA-nCeO₂ structure, and the improvement in compressive strength may be attributable to their structural integrity. The structure of Alg exhibited increased stiffness and Gel provided a matrix with a precise shape for cell adhesion and value addition.^{56,62} Mechanical strength was substantially impacted by the hydrogel scaffold's porosity and degree of cross-linking.^{63,64} In addition to preventing the irreversible hydrolysis of Gel, using cationic cross-linked Gel gives it more mechanical strength than the simple Gel fraction. This is most likely because an ester bond forms between the hydroxyl and carboxyl groups of the Alg and an amide bond between the carboxyl and amino groups.

Cell Proliferation and Morphology of MC3T3-E1 Cells on the GA-nCeO₂ Hydrogel Scaffold

In this study, MC3T3-E1 cells were used as a model cell line to evaluate how osteoblasts responded to ceria and hydrogel scaffolds. Cell adhesion, diffusion, and proliferation are very strongly influenced by surface form, roughness, and wetting behavior. It is vital to select biomaterials for bone tissue implants that optimally encourage cell adhesion, migration, and expansion.^{53–55}

Bone tissue engineering scaffolds require good biocompatibility.^{65,66} The adherence and development of MC3T3-E1 cells on the scaffold were investigated in this work. After the third day of cell culture on the scaffold, each group's adherence and growth were examined at 500x magnification (Figure 4A–D). The figure shows that although there were variations in the extension status, cell adhesion was evident in each group of scaffolds. The 3D structure of the GA-nCeO₂ hydrogel scaffold may be responsible for cell adhesion. Hydrogel porosity is crucial because large surface areas encourage cell attachment and ingrowth.⁶⁷ Figure 4A depicts the cell attachment to the Alg scaffold with prominently projecting nuclei. Numerous cells could cling to Gel scaffolds with good development, as illustrated in Figure 4B. Cell extension and adhesion were more pronounced in GA-nCeO₂ hydrogels than in other groups as they developed more uniformly with thick and lengthy protrusions extending around them (shown by red arrows). This indicated that the surface roughness of the GA-nCeO₂ nanocomposite scaffold was increased by the addition of nCeO₂, improving cell adhesion.

Additionally, the proliferation of MC3T3-E1 cells on the scaffolds in each group was assessed using the CCK-8 assay. Figure 4E demonstrates how each group's MC3T3-E1 proliferation grew over time. The proliferation of MC3T3-E1 cells cultured on the GA-nCeO₂ hydrogel scaffolds was significantly faster than other groups ($p < 0.05$). In addition to labeling the MC3T3-E1 cells for life or death, responses of the cells to the four distinct hydrogel extract groups were also noted. Figure 4F–I showed that on the third day, the culture plates of all groups were covered with green fluorescence, indicating that the cells have survived and that the hydrogel extracts of different compositions have not adversely harmed the cells.

The GA-nCeO₂ scaffold consists of 1000 µg/mL of nCeO₂, which is the appropriate concentration for bone-building.²⁸ According to certain theories, nCeO₂ might enhance cell development in degradable polymer matrices because it has dual-

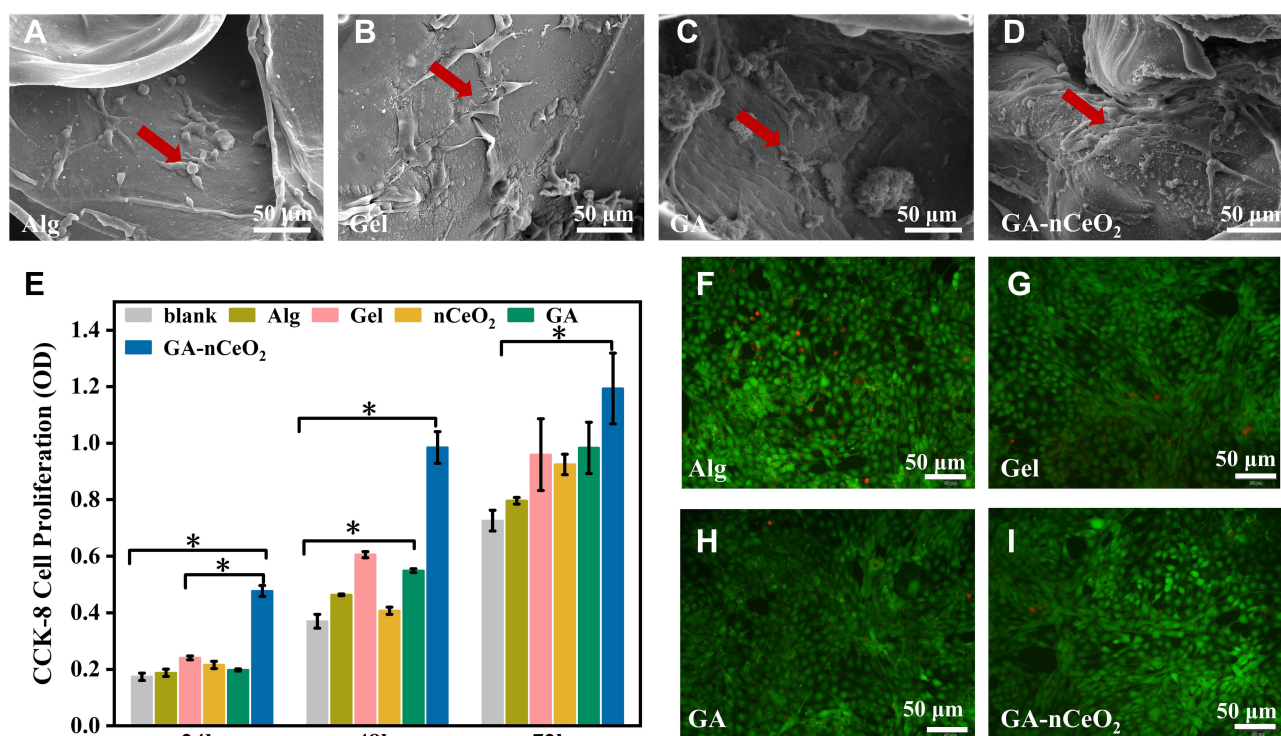


Figure 4 In vitro biocompatibility of MC3T3-E1 cells on the hydrogel scaffold: (A–D) the SEM images of MC3T3-E1 cells cultured on the Alg, Gel, GA, and GA-nCeO₂ hydrogel scaffold for 3 days (red arrows showed cells stretched by adhesion on hydrogels); (E) CCK-8 assay for cells cultured for 1, 2, and 3 days on Alg, Gel, GA, and GA-nCeO₂ hydrogel scaffold; (F–I) Live and dead staining for cells on Alg, Gel, GA, and GA-nCeO₂ hydrogel scaffold at 3 days. Scale bar: 50µm. The asterisks indicate a statistically significant difference from the groups (**p* < 0.05).

oxidation capabilities and its antioxidant mechanism could encourage cell adhesion and proliferation.¹¹ This might be attributed to the Ce⁴⁺/Ce³⁺ ratio of nCeO₂, which has a strong antioxidant activity and promotes cell proliferation when the ratio is high (Figure 1F). The pores created by the lyophilization of the material offer the cells with pathways for exchanging nutrients and metabolites, which was one of the factors contributing to cell adherence and proliferation.⁶⁸ As the hydrogel scaffold degrades, the exposed negatively charged nCeO₂ (Figure 1C) could modify protein adsorption, alter integrin-matrix interactions on the surface, pull positively charged ions from the surrounding medium, and encourage cell adhesion and proliferation. Previous studies looked at the function of Ce valence in osteoblasts and examined how the cell adheres to Ce⁴⁺ and Ce³⁺. Cell shape and diffusion could be directly altered by changes in Ce valence. Ce⁴⁺ is often a stable valence state in nCeO₂ (Figure 1F). In Ce⁴⁺, it is easy to see how actin filament formation and vinculin activity occur. Significant activity is present in dot-filamentous pseudopodia in Ce⁴⁺.^{69,70} This finding suggested that filamentous pseudopodia play a function in cell environment sensing and create new adhesion connections that drive cell migration and diffusion. In addition, according to previous research, nCeO₂/Alg coatings showed an equivalent and continuous ability to effectively remove environmental ROS.³⁴ Superoxide anions created by adjacent cells may be eliminated by the unique enzyme activity of nCeO₂, which would also provide a microenvironment favorable to cell growth.

Mineralization of MC3T3-E1 Cells on GA-nCeO₂ Hydrogel Scaffold

Pro-osteoblastic MC3T3-E1 cells mineralize in vitro to produce significant extracellular calcium deposits. ALP activity, cell mineralization, and osteogenesis-related gene expression assays were used to assess osteoblast differentiation with Alg, Gel, nCeO₂, GA, and GA-nCeO₂. At days 7 there was no discernible difference between the GA-nCeO₂ hydrogel scaffold and GA groups, but much higher than the Alg and Gel hydrogel scaffold as shown in Figure 5A and B. However, at days 14, the ALP activity of the GA and GA-nCeO₂ scaffold materials dramatically increased. ALP activity was higher in GA-nCeO₂ scaffolds than in GA and other scaffolds. This result showed that MC3T3-E1 could differentiate into osteoblasts more quickly when nCeO₂ were added, and a greater number of cells did so. The results of the ALP activity assay on the GA-

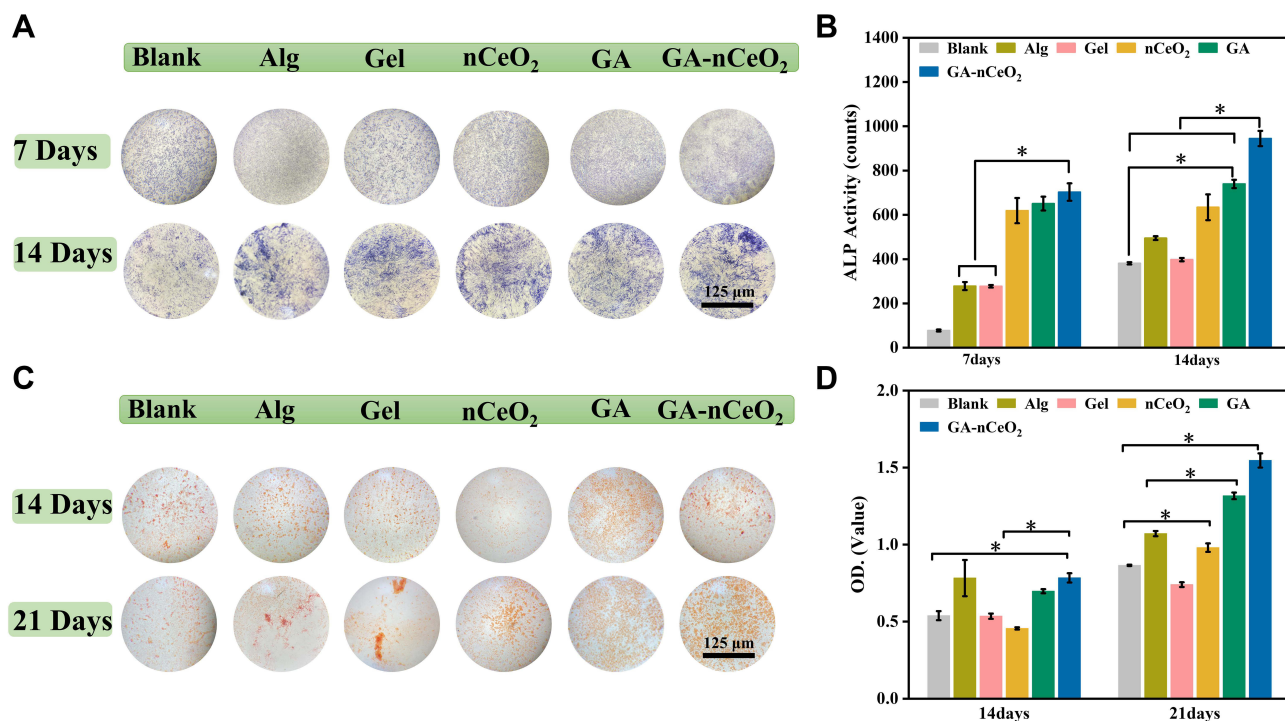


Figure 5 ALP Activity Measurements and Cell Mineralization: (A) ALP staining images at 7 and 14 days; (B) ALP activity of cells cultured on hydrogel scaffold for 7 and 14 days. (C) ARS-stained images at 14 and 21 days; (D) mineralization of cells cultured on hydrogel scaffold for 14 and 21 days. Scale bar: (A and C) 125 μ m. The asterisks indicate a statistically significant difference from the groups (* $p < 0.05$).

nCeO₂ scaffold showed that it was still active after 14 days, indicating that osteoblasts were actively driving the mineralization process before induction. Figure 5C and D depicted the mineralization of cells at 14 and 21 days, which is a sign of late osteogenic development in cells. Furthermore, compared to the other four groups, GA-nCeO₂ scaffolds showed the highest cell mineralization (a sign of late osteogenesis) (Figure 5D). This result demonstrated that the potential of MC3T3-E1 cells to stimulate bone formation was well enhanced by the addition of nCeO₂.

The osteogenic gene expression generated by the GA-nCeO₂ hydrogel scaffold is shown in Figure 6A. Widely used early indicators in the differentiation of osteoblasts were Runx-2 and ALP.⁷¹ It has been demonstrated that Runx-2 controls the transcription of genes involved in osteogenic differentiation in the MC3T3-E1 cell line during the early stages of osteogenesis. Runx-2 gene expression levels are significantly correlated with osteoblast activity and osteogenic differentiation. As shown in Figure 6B–D, Runx-2 expression at days 7, 14, and 21 in GA and GA-nCeO₂ scaffolds was assessed. Compared to days 7, the expression of Runx-2 was increased on day 14. Runx-2 levels were greater in GA-nCeO₂ scaffolds than in nCeO₂ and GA scaffolds at 14 days ($p < 0.05$). ALP gene expression steadily reduced from 14 to 21 days, which was in line with reports that ALP activity gradually declined throughout the transition from osteoblasts to osteogenesis. When combined with the ALP assay in the upper part, the elevation of the early marker ALP from 7 to 14 days demonstrated the significance of GA-nCeO₂ scaffolds in the early differentiation of bone. It was evident from the XPS examination of the nCeO₂ and GA-nCeO₂ scaffolds (Figures 1E, 1F and 3D) that nCeO₂ existed in both valence states. The degradation of the GA-nCeO₂ scaffold increases over time, exposing more nCeO₂. The high Ce⁴⁺/Ce³⁺ ratio in the early stage caused nCeO₂ to demonstrate catalytic activity, which removes ROS from cells and speeds up osteoblast differentiation. Additionally, nCeO₂ may stimulate the bone morphogenetic protein (BMP) signaling pathway and interact with bone morphogenetic protein receptor (BMPR) to promote the production of Smad proteins that have been phosphorylated.^{72,73} Then smad1/5/8 expression is further activated by nCeO₂, which activates the BMP signaling pathway and interacts with the BMPR and p-Smad1/5/8 binds to Smad4, leading to upregulation of the osteogenic master transcription factor Runx-2.

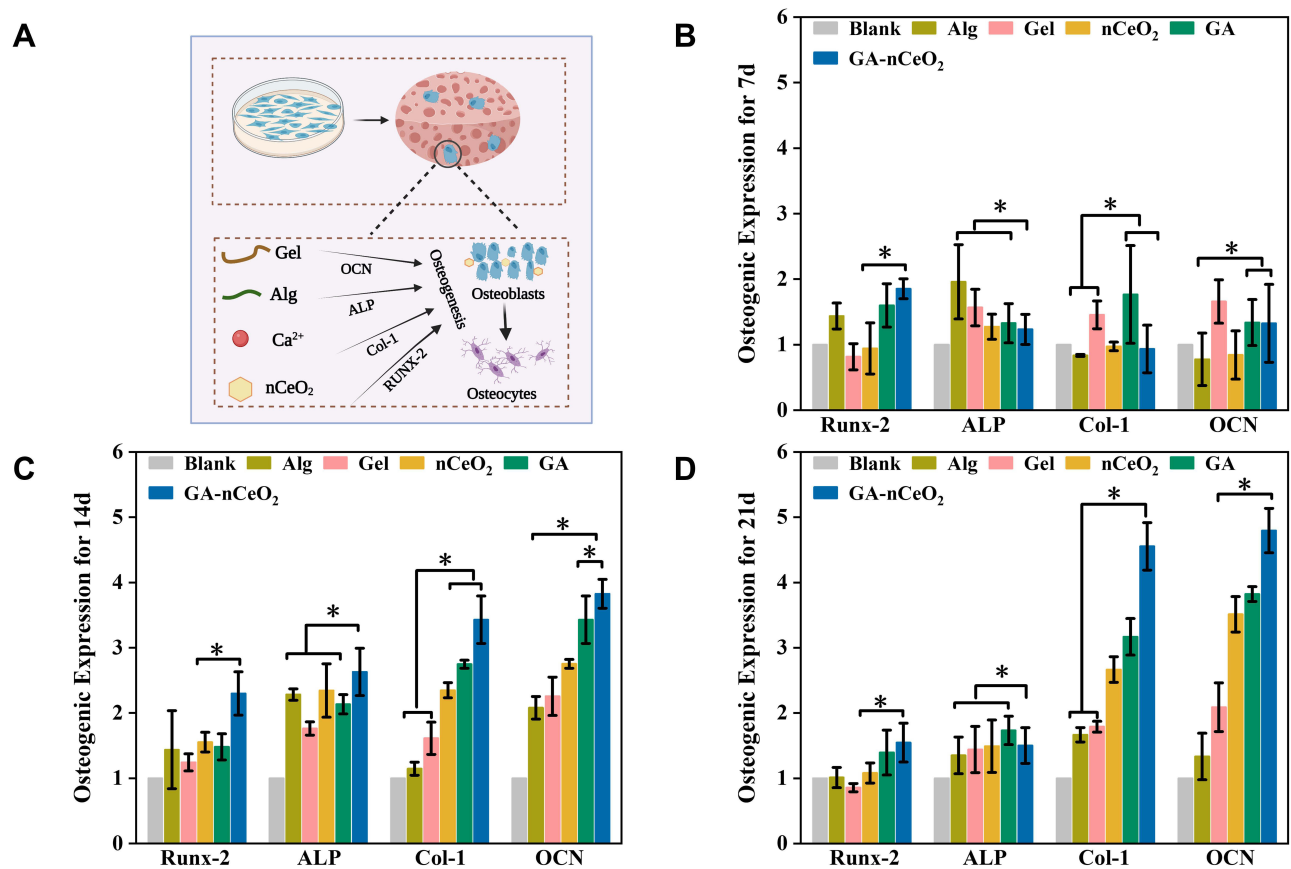


Figure 6 Osteogenic gene expression of MC3T3-E1 cells cultured on the hydrogel scaffold: **(A)** The illustration of the gene expression on GA-nCeO₂ hydrogel scaffold; **(B)** relative osteogenic gene expression of cells after culturing on the hydrogels for 7 days; **(C)** relative osteogenic gene expression of cells after culturing on the hydrogels for 14 days; **(D)** relative osteogenic gene expression of cells after culturing on the hydrogels for 21 days.

Notes: Runt-related transcription factor 2 (Runx-2), alkaline phosphatase activity (ALP), collagen type I (Col-1), osteocalcin (OCN). In **(B–D)**, osteogenic gene expression of MC3T3-E1 on culture disks without hydrogels was used as the calibrator. The asterisks indicate a statistically significant difference from the groups (**p* < 0.05).

Col-1, a protein in the extracellular matrix, promotes osteoblast adhesion and development and aids in bone maintenance and repair. At day 21, it was discovered that the levels of Col-1 in the GA-nCeO₂ group were significantly greater than those in the GA group. This difference may have resulted from the addition of nCeO₂, which made the scaffold's surface rougher and more increased the amount of collagen expressed on that surface. Moreover, it has been demonstrated that OCN, a marker of the stage of bone mineralization, can be expressed in mature osteoblasts. It is interesting to see that OCN expression grew with time in every group. Similarly, compared to GA scaffolds, the GA-nCeO₂ hydrogel scaffold produced larger quantities of OCN. This result may also point to the possibility that nCeO₂ exposure could activate calcium-sensing receptors, resulting in increased OCN expression.⁷⁴ The results of the mineralization levels were consistent with the upregulation of OCN levels and enhanced mineralization of bone tissue. MC3T3-E1 cells develop along a porous, three-dimensional structure that has a sizable spreading region and a more stretched cytoplasm. As a result, cytoskeleton is mechanically stimulated by alteration in cell morphology and deformed. This deformation is transmitted to the interior of the cell by appropriate proteins in the cell membrane, activating a number of downstream signaling pathways that have an impact on the biological behavior of cell proliferation and differentiation. The differentiation of bone marrow mesenchymal cells into osteoblasts was additionally aided by activation of the osteogenic master transcription factor Runx-2, which subsequently promotes the osteoblast marker genes Col-1 and OCN. Our preliminary study showed that, when compared to other groups, the composite GA-nCeO₂ hydrogel scaffold might increase the proliferation and osteogenic differentiation of MC3T3-E1 cells. This was supported by the expression of important osteogenic genes.

Biocompatibility and Degradation of GA-nCeO₂ Hydrogel Scaffold in vivo

Figure 7 shows how the biocompatibility, degradation, and bone formation of the GA-nCeO₂ hydrogel scaffold were examined in vivo using a rat femoral lesion model. Femoral samples were obtained for microscopic and gross inspection (Figure 7B and C). Remains of the rat femur scaffold 4, 6, and 8 weeks after surgery showed that the GA-nCeO₂ hydrogel scaffold could steadily disintegrate in vivo. Even at week 8, the scaffold was essentially degraded (Figure 7B). At the week 4, it was clear that the control group's defect surface was marginally higher than that of the experimental group. This is further supported by micro-CT measurements of the amount of new bone growth in the femur (Figure 7C). The regenerated bone at the defect increased with the passage of time in the two groups, but there was little difference between the two groups at the week 6. However, in comparison to the control group, the GA-nCeO₂ hydrogel scaffold group was higher during the week 8. To establish trustworthy parameters for bone regeneration of femoral lesions, quantitative morphological data acquired from micro-CT images were examined in accordance with bone surface area/bone volume (BS/TV) and bone volume/total volume (BV/TV). When comparing the two groups at the week 4 after the operation, Figure 7D and E revealed a significant difference in bone formation, including BV/TV and BS/TV, which was lower in the experimental group than that in the control group ($p < 0.05$). This might be because the hydrogel scaffold takes some time to degrade in vivo. The degradation of hydrogel could promote the exposure of nCeO₂. Since Ce⁴⁺ and Ce³⁺ alternatively gain and lose electrons, nCeO₂ has been shown to have the capacity to stimulate proliferation and osteogenic differentiation. Therefore, as time went on, the exposure of nCeO₂ grew and the GA-nCeO₂ group's bone regeneration outperformed that of the control group (Figure 7D and E).

Subsequently, H&E and Masson staining were performed to observe the degradation of the hydrogels in vivo and the concomitant bone regeneration at the week 4, 6, and 8, respectively. The femoral defects at all time points did not regenerate completely, and the unrepaired areas were occupied by connective tissue, as shown by the H&E staining results (Figure 8A–8E). H&E and Masson's trichrome-stained image at the week 8 postoperatively (Figure 8A–D and F–I) showed the significant new bone deposition at the edge of the defect area. As shown in Figure 8E and J, further quantitative analysis of

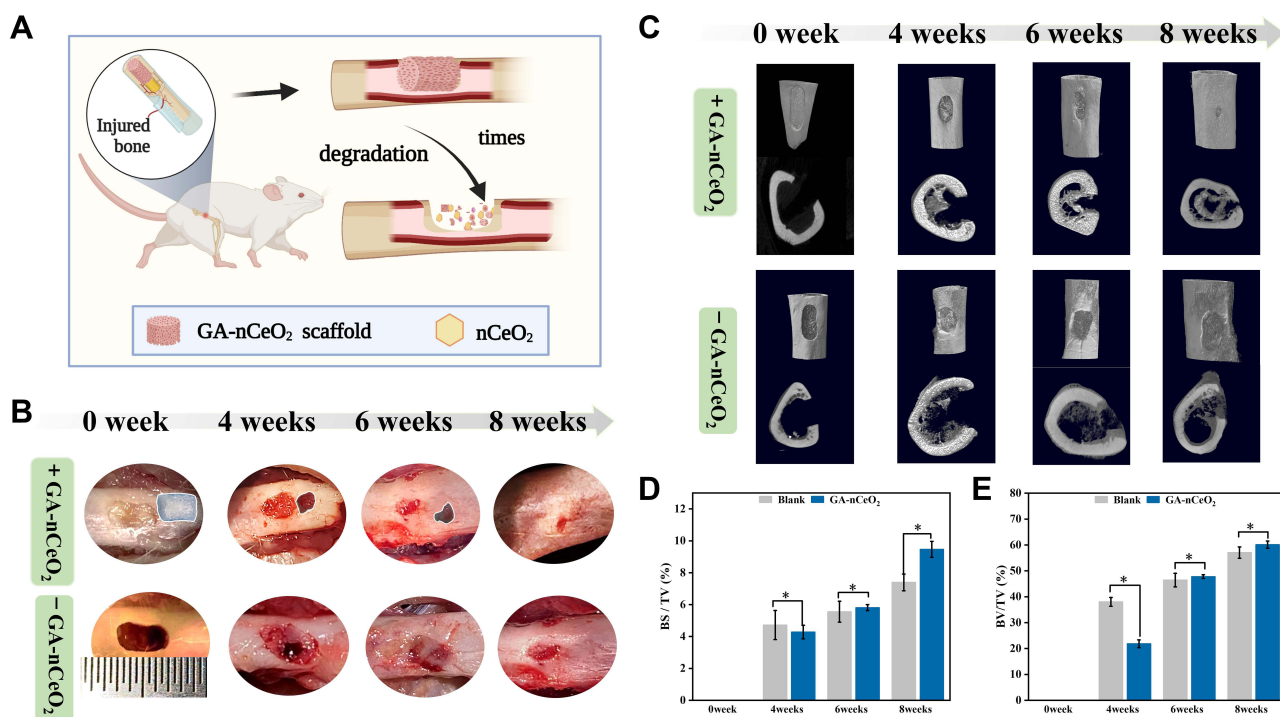


Figure 7 Biocompatibility and degradation of GA-nCeO₂ hydrogel scaffold for bone defects in vivo: (A) The illustration of the degradation of GA-nCeO₂ hydrogel scaffold in vivo; (B) Representative animal images of the implantation with GA-nCeO₂ hydrogel scaffold or without GA-nCeO₂ hydrogel scaffold at the week 4, 6 and 8; (C) Micro-CT images of the implantation with GA-nCeO₂ hydrogel scaffold or without GA-nCeO₂ hydrogel scaffold at the week 4, 6 and 8; (D) Bone surface area/bone volume (BS/TV); (E) Bone volume/total volume (BV/TV). The asterisks indicate a statistically significant difference from the groups (* $p < 0.05$).

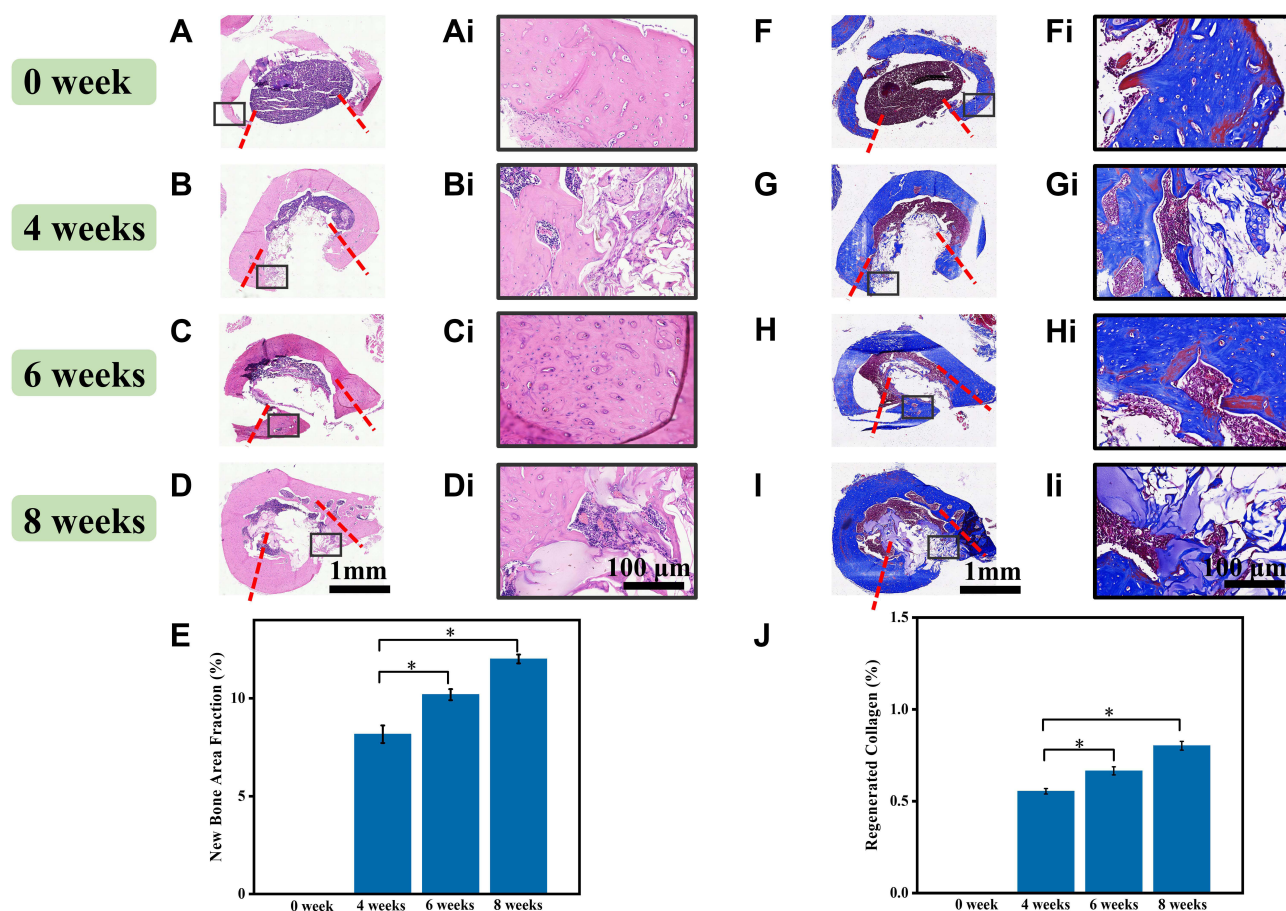


Figure 8 Representative H&E staining (A–D) and Masson’s trichrome staining (F–I) analysis after implantation in vivo with different times: (A, Ai, F, and Fi) 0 weeks; (B, Bi, G, and Gi) 4 weeks; (C, Ci, H, and Hi) 6 weeks and (D, Di, I, and Ii) 8 weeks. As shown in (A–D, F–I), the periosteal side was on the top, while the dura side was at the bottom. The images of the black rectangle areas in (A–D) and (F–I) were magnified in (Ai–Di) and (Fi–Ii), respectively. Scale bar: (A–D, F–I) 1 mm, (Ai–Di, Fi–Ii) 100 μ m. Histomorphometrically analysis of (E) new bone area fraction and (J) regenerated collagen. The asterisks indicate a statistically significant difference from the groups (* $p < 0.05$).

H&E and Masson’s trichrome-stained image showed that the area of new bone formation and collagen deposition in GA-nCeO₂ hydrogel scaffold increased significantly at the week 8 postoperatively ($p < 0.05$).

The GA-nCeO₂ hydrogel scaffold’s high mechanical strength and biocompatibility make them potentially non-cytotoxic biomaterials for bone tissue regeneration. The intermolecular synergy between nCeO₂ and the GA scaffold improves cell adhesion, proliferation, survival, and differentiation on the scaffold surface. Overall, the dual-oxidation states and the optimized crystal structure of nCeO₂, as well as the three-dimensional porous scaffold resembling an extracellular matrix, may be responsible for the good osteogenic properties of GA-nCeO₂ hydrogel scaffold, highlighting the enormous potential for bone tissue regeneration applications.

Conclusions

Gel, Alg, and nCeO₂-based nanocomposite hydrogel scaffolds were successfully produced by lyophilization. The effective binding of nCeO₂ to GA complexes was revealed by analyzing the swelling behavior, in vitro degradation behavior and mechanical strength analysis. It is interesting to note that GA scaffolds and nCeO₂ work together synergistically to promote cell adhesion and proliferation. Furthermore, the GA-nCeO₂ hydrogel scaffold promoted the osteogenic differentiation of MC3T3-E1 cells. Our in vivo biocompatibility and degradation test in rats showed that GA-nCeO₂ hydrogel scaffold demonstrated excellent properties as a potential bone tissue engineering scaffold, especially for bone defect.

Ethics Approval and Informed Consent

Femoral defect models were created in 4-week-old male SD rats following a protocol approved by the Institutional Animal Ethics Committee of Qingdao University Laboratory Animal Center (20210708SD1520210920064) and were conducted in strict accordance with the Guidelines for Ethical Review of Laboratory Animal Welfare in China (GB/T35892-2018). Briefly, the rat was anesthetized by isoflurane inhalation and a 2 cm linear incision was made in the proximal femur.

Acknowledgments

The work was supported by the Shandong Provincial Natural Science Foundation Youth Project (ZR2021QH251) and Clinical Medicine +X Research Project of Affiliated Hospital of Qingdao University (QDFY+X2021055).

Author Contributions

All authors made substantial contributions to the design and conception of the study and acquisition, analysis, and interpretation of data and took part in either drafting or revising the manuscript. All authors gave final approval for the version to be published, have agreed on the journal to which the article has been submitted, and agreed to be accountable for all aspects of the work in ensuring that questions related to the accuracy or integrity of any part of the work are appropriately investigated and resolved.

Disclosure

There are no conflicts of interest to declare.

References

1. Zhu G, Zhang T, Chen M, et al. Bone physiological microenvironment and healing mechanism: basis for future bone-tissue engineering scaffolds. *Bioact Mater*. 2021;6(11):4110–4140. doi:10.1016/j.bioactmat.2021.03.043
2. Zhu J, Zhang C, Jia J, et al. Osteogenic effects in a rat osteoporosis model and femur defect model by simvastatin microcrystals. *Ann N Y Acad Sci*. 2021;1487(1):31–42. doi:10.1111/nyas.14513
3. Boateng J, Burgos-Amador R, Okeke O, Pawar H. Composite alginate and gelatin based bio-polymeric wafers containing silver sulfadiazine for wound healing. *Int J Biol Macromol*. 2015;79:63–71. doi:10.1016/j.ijbiomac.2015.04.048
4. Hoffman AS. Hydrogels for biomedical applications. *Adv Drug Deliv Rev*. 2012;64:18–23. doi:10.1016/j.addr.2012.09.010
5. Lim JYC, Lin Q, Xue K, Loh XJ. Recent advances in supramolecular hydrogels for biomedical applications. *Mater Today Adv*. 2019;3:100021. doi:10.1016/j.mtadv.2019.100021
6. Mogoşanu GD, Grumezescu AM. Natural and synthetic polymers for wounds and burns dressing. *Int J Pharm*. 2014;463(2):127–136. doi:10.1016/j.ijpharm.2013.12.015
7. Łabowska MB, Cierluk K, Jankowska AM, Kulbacka J, Detyna J, Michalak I. A review on the adaption of alginate-gelatin hydrogels for 3D cultures and bioprinting. *Materials*. 2021;14(4):858. doi:10.3390/ma14040858
8. Giuseppe MD, Law N, Webb B, et al. Mechanical behaviour of alginate-gelatin hydrogels for 3D bioprinting. *J Mech Behav Biomed Mater*. 2018;79:150–157. doi:10.1016/j.jmbm.2017.12.018
9. Sharma C, Dinda AK, Potdar PD, Chou CF, Mishra NC. Fabrication and characterization of novel nano-biocomposite scaffold of chitosan–gelatin–alginate–hydroxyapatite for bone tissue engineering. *Mater Sci Eng C*. 2016;64:416–427. doi:10.1016/j.msec.2016.03.060
10. Faramarzi N, Yazdi IK, Nabavinia M, et al. Patient-specific bioinks for 3D bioprinting of tissue engineering scaffolds. *Adv Healthcare Mater*. 2018;7(11):1701347. doi:10.1002/adhm.201701347
11. El Fray M, Strzalkowska D, Mandoli C, Pagliari F, Di Nardo P, Traversa E. Influence of ceria nanoparticles on chemical structure and properties of segmented polyesters. *Mater Sci Eng C*. 2015;53:15–22. doi:10.1016/j.msec.2015.04.010
12. Cao Y, Yang S, Zhao D, et al. Three-dimensional printed multiphasic scaffolds with stratified cell-laden gelatin methacrylate hydrogels for biomimetic tendon-to-bone interface engineering. *J Orthop Translat*. 2020;23:89–100. doi:10.1016/j.jot.2020.01.004
13. Panouillé M, Larreta-Garde V. Gelation behaviour of gelatin and alginate mixtures. *Food Hydrocoll*. 2009;23(4):1074–1080. doi:10.1016/j.foodhyd.2008.06.011
14. Ferris CJ, Gilmore KJ, Beirne S, McCallum D, Wallace GG. Bio-ink for on-demand printing of living cells. *Biomater Sci*. 2013;1(2):224–230. doi:10.1039/C2BM00114D
15. Yuan L, Wu Y, Gu QS, El-Hamshary H, El-Newehy M, Mo X. Injectable photo crosslinked enhanced double-network hydrogels from modified sodium alginate and gelatin. *Int J Biol Macromol*. 2017;96:569–577. doi:10.1016/j.ijbiomac.2016.12.058
16. Grenier J, Duval H, Barou F, Lv P, David B, Letourneur D. Mechanisms of pore formation in hydrogel scaffolds textured by freeze-drying. *Acta Biomaterialia*. 2019;94:195–203. doi:10.1016/j.actbio.2019.05.070
17. Feng P, Wang K, Shuai Y, Peng S, Hu Y, Shuai C. Hydroxyapatite nanoparticles in situ grown on carbon nanotube as a reinforcement for poly (ϵ -caprolactone) bone scaffold. *Mater Today Adv*. 2022;15:100272. doi:10.1016/j.mtadv.2022.100272
18. Gan D, Jiang Y, Hu Y, et al. Mussel-inspired extracellular matrix-mimicking hydrogel scaffold with high cell affinity and immunomodulation ability for growth factor-free cartilage regeneration. *J Orthop Translat*. 2022;33:120–131. doi:10.1016/j.jot.2022.02.006

19. Iranmanesh P, Gowdini M, Khademi A, et al. Bioprinting of three-dimensional scaffold based on alginate-gelatin as soft and hard tissue regeneration. *J Mater Res Technol.* 2021;14:2853–2864. doi:10.1016/j.jmrt.2021.08.069
20. Cheng Y, Morovvati MR, Huang M, et al. A multilayer biomimetic chitosan-gelatin-fluorohydroxyapatite cartilage scaffold using for regenerative medicine application. *J Mater Res Technol.* 2021;14:1761–1777. doi:10.1016/j.jmrt.2021.07.052
21. Li X, Saeed SS, Beni MH, et al. Experimental measurement and simulation of mechanical strength and biological behavior of porous bony scaffold coated with alginate-hydroxyapatite for femoral applications. *Compos Sci Technol.* 2021;214:108973. doi:10.1016/j.compscitech.2021.108973
22. Kalyanaraman V, Naveen SV, Mohana N, et al. Biocompatibility studies on cerium oxide nanoparticles – combined study for local effects, systemic toxicity and genotoxicity via implantation route. *Toxicol Res.* 2019;8(1):25–37. doi:10.1039/C8TX00248G
23. Ferraro D, Tredici IG, Ghigna P, et al. Dependence of the Ce(III)/Ce(IV) ratio on intracellular localization in ceria nanoparticles internalized by human cells. *Nanoscale.* 2017;9(4):1527–1538. doi:10.1039/c6nr07701c
24. Yuan K, Mei J, Shao D, et al. Cerium oxide nanoparticles regulate osteoclast differentiation bidirectionally by modulating the cellular production of reactive oxygen species. *IJN.* 2020;15:6355–6372. doi:10.2147/IJN.S257741
25. Li J, Wen J, Li B, et al. Valence state manipulation of cerium oxide nanoparticles on a titanium surface for modulating cell fate and bone formation. *Adv Sci.* 2018;5(2):1700678. doi:10.1002/adv.201700678
26. Wei F, Neal CJ, Sakthivel TS, Kean T, Seal S, Coathup MJ. Multi-functional cerium oxide nanoparticles regulate inflammation and enhance osteogenesis. *Mater Sci Eng C.* 2021;124:112041. doi:10.1016/j.msec.2021.112041
27. You M, Li K, Xie Y, Huang L, Zheng X. The effects of cerium valence states at cerium oxide coatings on the responses of bone mesenchymal stem cells and macrophages. *Biol Trace Elem Res.* 2017;179(2):259–270. doi:10.1007/s12011-017-0968-4
28. Purohit SD, Singh H, Bhaskar R, et al. Gelatin–alginate–cerium oxide nanocomposite scaffold for bone regeneration. *Mater Sci Eng C.* 2020;116:111111. doi:10.1016/j.msec.2020.111111
29. Gupta A, Sakthivel TS, Neal CJ, et al. Antioxidant properties of ALD grown nanocerium films with tunable valency. *Biomater Sci.* 2019;7(7):3051–3061. doi:10.1039/c9bm00397e
30. Zhou Z, Cui J, Wu S, Geng Z, Su J. Silk fibroin-based biomaterials for cartilage/osteochondral repair. *Theranostics.* 2022;12(11):5103–5124. doi:10.7150/thno.74548
31. Purohit SD, Bhaskar R, Singh H, Yadav I, Gupta MK, Mishra NC. Development of a nanocomposite scaffold of gelatin–alginate–graphene oxide for bone tissue engineering. *Int J Biol Macromol.* 2019;133:592–602. doi:10.1016/j.ijbiomac.2019.04.113
32. Nanda HS. Surface modification of promising cerium oxide nanoparticles for nanomedicine applications. *RSC Adv.* 2016;6(113):111889–111894. doi:10.1039/C6RA23046F
33. Li X, Qi M, Sun X, et al. Surface treatments on titanium implants via nanostructured ceria for antibacterial and anti-inflammatory capabilities. *Acta Biomaterialia.* 2019;94:627–643. doi:10.1016/j.actbio.2019.06.023
34. Dutta D, Mukherjee R, Ghosh S, Patra M, Mukherjee M, Basu T. Cerium oxide nanoparticles as antioxidant or pro-oxidant agents. *ACS Appl Nano Mater.* 2022;5(1):1690–1701. doi:10.1021/acsanm.1c04518
35. Heckert EG, Karakoti AS, Seal S, Self WT. The role of cerium redox state in the SOD mimetic activity of nanocerium. *Biomaterials.* 2008;29(18):2705–2709. doi:10.1016/j.biomaterials.2008.03.014
36. Hussain M, Suo H, Xie Y, et al. Dopamine-substituted multidomain peptide hydrogel with inherent antimicrobial activity and antioxidant capability for infected wound healing. *ACS Appl Mater Interfaces.* 2021;13(25):29380–29391. doi:10.1021/acsami.1c07656
37. Jamnezhad S, Asefnejad A, Motifard M, et al. Development and investigation of novel alginate-hyaluronic acid bone fillers using freeze drying technique for orthopedic field. *Nanomed Res J.* 2020;5(4):306–315. doi:10.22034/nmrj.2020.04.001
38. Soleimani M, Asgharzadeh Salmasi A, Asghari S, et al. Optimization and fabrication of alginate scaffold for alveolar bone regeneration with sufficient drug release. *Int Nano Lett.* 2021;11(3):295–305. doi:10.1007/s40089-021-00342-0
39. Nazmi NN, Isa MIN, Sarbon NM. Preparation and characterization of chicken skin gelatin/CMC composite film as compared to bovine gelatin film. *Food Biosci.* 2017;19:149–155. doi:10.1016/j.fbio.2017.07.002
40. Kurtuldu F, Mutlu N, Michálek M, et al. Cerium and gallium containing mesoporous bioactive glass nanoparticles for bone regeneration: bioactivity, biocompatibility and antibacterial activity. *Mater Sci Eng C Mater Biol Appl.* 2021;124:112050. doi:10.1016/j.msec.2021.112050
41. Luo J, Zhu S, Tong Y, et al. Cerium oxide nanoparticles promote osteoplastic precursor differentiation by activating the Wnt pathway. *Biol Trace Elem Res.* 2022. doi:10.1007/s12011-022-03168-9
42. Wang QQ, Liu Y, Zhang CJ, Zhang C, Zhu P. Alginate/gelatin blended hydrogel fibers cross-linked by Ca²⁺ and oxidized starch: preparation and properties. *Mater Sci Eng C.* 2019;99:1469–1476. doi:10.1016/j.msec.2019.02.091
43. Staroszczyk H, Sztuka K, Wolska J, Wojtasz-Pajak A, Kołodziejaska I. Interactions of fish gelatin and chitosan in uncrosslinked and crosslinked with EDC films: FT-IR study. *Spectrochim Acta Part A.* 2014;117:707–712. doi:10.1016/j.saa.2013.09.044
44. Mathew M, Rad MA, Mata JP, et al. Hyperbranched polymers tune the physicochemical, mechanical, and biomedical properties of alginate hydrogels. *Mater Today Chem.* 2022;23:100656. doi:10.1016/j.mtchem.2021.100656
45. Derkach SR, Voronko NG, Sokolan NI, Kolotova DS, Kuchina YA. Interactions between gelatin and sodium alginate: UV and FTIR studies. *J Dispers Sci Technol.* 2020;41(5):690–698. doi:10.1080/01932691.2019.1611437
46. Thanos C, Bintz B, Bell W, et al. Intraperitoneal stability of alginate–polyornithine microcapsules in rats: an FTIR and SEM analysis. *Biomaterials.* 2006;S0142961206001311. doi:10.1016/j.biomaterials.2006.01.042
47. Elkhoshkhany N, Khatab MA, Kabary MA, Thermal FTIR. UV spectral studies on tellurite glasses doped with cerium oxide. *Ceram Int.* 2018;44(3):2789–2796. doi:10.1016/j.ceramint.2017.11.019
48. Mihaylov MY, Ivanova EZ, Vayssilov GN, Hadjiivanov KI. Revisiting ceria-NO_x interaction: FTIR studies. *Catal Today.* 2020;357:613–620. doi:10.1016/j.cattod.2019.05.014
49. Singh A, Hussain I, Singh NB, Singh H. Uptake, translocation and impact of green synthesized nanocerium on growth and antioxidant enzymes activity of *Solanum lycopersicum* L. *Ecotoxicol Environ Saf.* 2019;182:109410. doi:10.1016/j.ecoenv.2019.109410
50. Shlapa Y, Timashkov I, Veltruska K, et al. Structural and physical-chemical characterization of redox active CeO nanoparticles synthesized by precipitation in water-alcohol solutions. *Nanotechnology.* 2021;32(31):315706. doi:10.1088/1361-6528/abf7e9
51. Baldim V, Bedioui F, Mignet N, Margail I, Berret JF. The enzyme-like catalytic activity of cerium oxide nanoparticles and its dependency on Ce³⁺ surface area concentration. *Nanoscale.* 2018;10(15):6971–6980. doi:10.1039/C8NR00325D

52. Abdel-Mageed HM, Abd El Aziz AE, Abdel RBM, Mohamed SA, Nada D. Antioxidant-biocompatible and stable catalase-based gelatin–alginate hydrogel scaffold with thermal wound healing capability: immobilization and delivery approach. *Biotech.* 2022;12(3):73. doi:10.1007/s13205-022-03131-4
53. Seminko V, Maksimchuk P, Grygorova G, et al. Mechanism and dynamics of fast redox cycling in cerium oxide nanoparticles at high oxidant concentration. *J Phys Chem C.* 2021;125(8):4743–4749. doi:10.1021/acs.jpcc.1c00382
54. Nelson BC, Johnson ME, Walker ML, Riley KR, Sims CM. Antioxidant cerium oxide nanoparticles in biology and medicine. *Antioxidants.* 2016;5(2):15. doi:10.3390/antiox5020015
55. Yao B, Hu T, Cui X, Song W, Fu X, Huang S. Enzymatically degradable alginate/gelatin bioink promotes cellular behavior and degradation $\$less\$in vitro\$less\$i\$greater\$ and $\$less\$i\$greater\$in vivo\$less\$i\$greater\$$. *Biofabrication.* 2019;11(4):045020. doi:10.1088/1758-5090/ab38ef$$
56. Gómez-Guillén MC, Giménez B, López-Caballero ME, Montero MP. Functional and bioactive properties of collagen and gelatin from alternative sources: a review. *Food Hydrocoll.* 2011;25(8):1813–1827. doi:10.1016/j.foodhyd.2011.02.007
57. Sornkamnerd S, Okajima MK, Tough KT. Porous hydrogels prepared by simple lyophilization of LC gels. *ACS Omega.* 2017;2(8):5304–5314. doi:10.1021/acsomega.7b00602
58. Ahmed EM. Hydrogel: preparation, characterization, and applications: a review. *J Adv Res.* 2015;6(2):105–121. doi:10.1016/j.jare.2013.07.006
59. Xue X, Hu Y, Wang S, Chen X, Jiang Y, Su J. Fabrication of physical and chemical crosslinked hydrogels for bone tissue engineering. *Bioact Mater.* 2022;12:327–339. doi:10.1016/j.bioactmat.2021.10.029
60. Feng P, Wu P, Gao C, et al. A multimaterial scaffold with tunable properties: toward bone tissue repair. *Adv Sci.* 2018;5(6):1700817. doi:10.1002/advs.201700817
61. Zou Y, Huang B, Cao L, Deng Y, Su J. Tailored mesoporous inorganic biomaterials: assembly, functionalization, and drug delivery engineering. *Adv Mater.* 2021;33(2):2005215. doi:10.1002/adma.202005215
62. Saunders PR, Ward AG. Mechanical properties of degraded gelatins. *Nature.* 1955;176(4470):26–27. doi:10.1038/176026a0
63. Yang C, Zheng Z, Younis MR, et al. 3D printed enzyme-functionalized scaffold facilitates diabetic bone regeneration. *Adv Funct Mater.* 2021;31(20):2101372. doi:10.1002/adfm.202101372
64. Zare-Harofteh A, Saber-Samandari S, Saber-Samandari S. The effective role of akermanite on the apatite-forming ability of gelatin scaffold as a bone graft substitute. *Ceram Int.* 2016;42(15):17781–17791. doi:10.1016/j.ceramint.2016.08.106
65. Shuai C, Yang W, Feng P, Peng S, Pan H. Accelerated degradation of HAP/PLLA bone scaffold by PGA blending facilitates bioactivity and osteoconductivity. *Bioact Mater.* 2021;6(2):490–502. doi:10.1016/j.bioactmat.2020.09.001
66. Mantripragada VP, Jayasuriya AC. Bone regeneration using injectable BMP-7 loaded chitosan microparticles in rat femoral defect. *Mater Sci Eng C.* 2016;63:596–608. doi:10.1016/j.msec.2016.02.080
67. Shuai C, Peng B, Feng P, Yu L, Lai R, Min A. In situ synthesis of hydroxyapatite nanorods on graphene oxide nanosheets and their reinforcement in biopolymer scaffold. *J Adv Res.* 2022;35:13–24. doi:10.1016/j.jare.2021.03.009
68. Pathak TS, Kim JS, Lee SJ, Baek DJ, Paeng KJ. Preparation of alginic acid and metal alginate from algae and their comparative study. *J Polym Environ.* 2008;16(3):198–204. doi:10.1007/s10924-008-0097-4
69. Naganuma T, Traversa E. The effect of cerium valence states at cerium oxide nanoparticle surfaces on cell proliferation. *Biomaterials.* 2014;35(15):4441–4453. doi:10.1016/j.biomaterials.2014.01.074
70. Krivosheeva O, Sababi M, Dedinaite A, Claesson PM. Nanostructured composite layers of mussel adhesive protein and ceria nanoparticles. *Langmuir.* 2013;29(30):9551–9561. doi:10.1021/la401693x
71. Guo L, Fan Y, Kawazoe N, Fan H, Zhang X, Chen G. Fabrication of gelatin-micropatterned surface and its effect on osteogenic differentiation of hMSCs. *J Mater Chem B.* 2018;6(7):1018–1025. doi:10.1039/C7TB03165C
72. Singh KR, Nayak V, Sarkar T, Singh RP. Cerium oxide nanoparticles: properties, biosynthesis and biomedical application. *RSC Adv.* 2020;10(45):27194–27214. doi:10.1039/D0RA04736H
73. Nadeem M, Khan R, Afridi K, et al. Green synthesis of cerium oxide nanoparticles (CeO₂ NPs) and their antimicrobial applications: a review. *Int J Nanomedicine.* 2020;15:5951–5961. doi:10.2147/IJN.S255784
74. Bellio P, Luzi C, Mancini A, et al. Cerium oxide nanoparticles as potential antibiotic adjuvant. Effects of CeO₂ nanoparticles on bacterial outer membrane permeability. *Biochim Biophys Acta Biomembr.* 2018;1860(11):2428–2435. doi:10.1016/j.bbmem.2018.07.002

International Journal of Nanomedicine

Dovepress

Publish your work in this journal

The International Journal of Nanomedicine is an international, peer-reviewed journal focusing on the application of nanotechnology in diagnostics, therapeutics, and drug delivery systems throughout the biomedical field. This journal is indexed on PubMed Central, MedLine, CAS, SciSearch®, Current Contents®/Clinical Medicine, Journal Citation Reports/Science Edition, EMBASE, Scopus and the Elsevier Bibliographic databases. The manuscript management system is completely online and includes a very quick and fair peer-review system, which is all easy to use. Visit <http://www.dovepress.com/testimonials.php> to read real quotes from published authors.

Submit your manuscript here: <https://www.dovepress.com/international-journal-of-nanomedicine-journal>